Chemical Science

ROYAL SOCIETY OF CHEMISTRY

EDGE ARTICLE

View Article Online
View Journal | View Issue

Cite this: *Chem. Sci.*, 2025, **16**, 19944

All publication charges for this article have been paid for by the Royal Society of Chemistry

Dual polarization in extended π-conjugated zwitterionic COF facilitates Li^+ aligned transportation for high-performance solid-state lithium–metal batteries

Linchu Xu,†[a] Feng Chen,†[a] Ju Duan,[a] Kexiang Wang,[a] Jiaqiang Li,[a] Jingzhao Wang,[b] Jianan Wang,[b] Wei Lyu *[a] and Yaozu Liao *[a]

Rational design of covalent organic frameworks (COFs) with tailored topology and multipolar characteristics offers a promising avenue for developing advanced composite electrolytes in high-rate solid-state lithium–metal batteries (SLMBs). Herein, we report an extended π-conjugated zwitterionic COF (QZwiCOF) that innovatively modulates the microstructure of PVDF-HFP to enable aligned Li^+ transport. The unique dual polarization induced by enhanced intramolecular charge transfer in QZwiCOF maximizes PVDF-HFP's dipole moment and structural regularity. Coupled with the amphiphilic nanochannel of QZwiCOF that provides Li^+-selective conduction, the resulting QZwiCOF-based composite electrolyte (ZiCP CPE) with merely 3 wt% QZwiCOF achieves enhanced ionic conductivity ($\sigma = 3.44 \times 10^{-4}$ S cm^{-1}), a high Li^+ transference number ($t_{Li^+} = 0.56$), improved mechanical and thermal stability. Consequently, a Li||NCM811 cell with ZiCP CPE achieves excellent rate performance, delivering a specific capacity of 145 mAh g^{-1} at 3.0C, much higher than that of a cell using PVDF-HFP SPE (51 mAh g^{-1}). Notably, even under 80 °C and 6.0C, it retains a capacity of 96 mAh g^{-1} after 200 cycles while the cell with PVDF-HFP SPE experiences a short circuit within 50 cycles, highlighting its potential for thermally resilient high-rate SLMBs. This work provides a molecular-level design strategy for engineering high-performance CPEs through zwitterionic COF-mediated ion channel regulation.

Received 28th July 2025
Accepted 18th September 2025

DOI: 10.1039/d5sc05645d

rsc.li/chemical-science

Introduction

Solid-state lithium metal batteries (SLMBs) offer superior safety and energy density, making them ideal for next-generation energy storage technology.[1] The rapid development of electric vehicles and portable electronic devices has driven the evolution of SLMBs toward high charging/discharging rates and superior stability.[2] However, practical implementation faces challenges including the sluggish bulk ion transport in solid-state polymer electrolytes (SPEs), interfacial side reactions during rapid charging/discharging cycling,[3] and thermal decomposition risks above 100 °C that may trigger thermal runaway.[4] According to Chazalviel theory,[5] optimizing SPEs requires both high free ion concentration and improved cation mobility to delay dendrite nucleation and extend battery life. Therefore, precisely regulating Li^+ electrochemical migration dynamics while enhancing thermodynamic stability is critical for achieving stable and high-rate SLMBs.

Extensive research efforts have focused on regulating Li^+ migration behavior in SPEs, including strategies such as polar polymer design,[6] crystallinity modulation,[7] and localized high-concentration salt engineering.[8] Despite these efforts, key limitations still persist, such as restricted ion transport due to excessive Li^+ binding affinity,[9] discontinuous Li^+ migration in disordered amorphous regions,[10] and interfacial side reactions caused by anion aggregation.[11] These factors together hinder the simultaneous attainment of fast ion transport and uniform deposition for achieving high-rate SLMBs. Recently, ordered porous materials, *e.g.*, metal–organic frameworks (MOFs) and covalent organic frameworks (COFs), have emerged as promising composite electrolytes candidates due to their tunable long-range ordered structures for directional Li^+ transport pathways.[12] Nevertheless, poor interfacial compatibility between porous fillers and polymer matrices typically restricts additive loading (<10 wt%),[13] rendering the ordered channels largely ineffective. Consequently, precisely constructing continuous and ordered ion transport channels in SPEs for high-rate SLMBs is still challenging.

Herein, we innovatively design an extended π-conjugated zwitterionic COF (QZwiCOF) featuring dual polarization to

[a]*State Key Laboratory of Advanced Fiber Materials, College of Materials Science and Engineering, Donghua University, Shanghai 201620, China. E-mail: yzliao@dhu.edu.cn*

[b]*Department of Environmental Engineering, Xi'an Key Laboratory of Solid Waste Recycling and Resource Recovery, School of Energy and Power Engineering, Xi'an Jiaotong University, Xi'an 710049, China*

† L. C. Xu and F. Chen contributed equally to this work.

regulate the microstructure of PVDF-HFP, enabling aligned Li^+ transport in SLMBs. Synthesized *via* a one-pot Povarov reaction, the quinoline-bridged skeletons endow QZwiCOF with enhanced π-electron delocalization, and feature functionalized covalently tethered imidazolium cation–sulfonate anion zwitterionic moieties. The unique molecular architecture of QZwiCOF induces dual polarization through intramolecular charge transfer (ICT) between sulfonate/imidazolium moieties (Δq = 0.19|*e*|) and quinoline backbone/imidazolium groups (Δq = 0.20|*e*|). Remarkably, this dual polarization significantly reorganizes the PVDF-HFP dipole alignment ($\mu_{PVDF\text{-}HFP}$ = 8.56 debye) and modulates chain orientation ($\Delta\Phi$ = +23°), as evidenced by the pronounced increase in TTTT conformation content from experimental analysis. Furthermore, the amphiphilic nanochannels of QZwiCOF can provide additional Li^+ coordination sites, while their electrostatic confinement effects suppress anion migration. This synergistic regulation endows the QZwiCOF-based composite electrolyte (ZiCP CPE) with improved ionic conductivity ($\sigma = 3.44 \times 10^{-4}$ S cm^{-1}), a high Li^+ transference number (t_{Li^+} = 0.56), enhanced mechanical strength (3.93 MPa), toughness (7.73 MJ m^{-3}), and flame retardancy, ensuring the high safety of the full cell. As a result, the assembled Li||NCM811 cell with ZiCP CPE shows remarkable rate performance, exhibiting a specific capacity of 145 mAh g^{-1} at 3.0C, much higher than that of a cell with PVDF-HFP SPE (51 mAh g^{-1}). Under 3.0C charging/discharging cycling, the cell achieves a specific capacity of 108 mAh g^{-1} with a high capacity retention rate of 87.8% after 200 cycles. Notably, owing to the flame retardancy of QZwiCOF, the cell operated at 80 °C and 6.0C still retains a capacity of 96 mAh g^{-1} after 200 cycles. This work gives insights into designing and developing high-performance CPEs with functionalized COFs for thermally resilient high-rate SLMBs.

Results and discussion

Molecular design and theoretical computations

Employing a multicomponent reaction (MCR) strategy, we precisely constructed the extended π-conjugated QZwiCOF *via* a one-pot Povarov reaction, in which 2,4,6-tris(4-aminophenyl) triazine (TATT), 1,3,5-tris(4-formylphenyl)triazine (TATB) and vinyl imidazole-based zwitterionic liquids (VZwILs) served as monomers (Fig. 1a and S1). The formed electron-deficient quinoline acceptor units endow QZwiCOF with an extended π-conjugation and enhanced π-electron delocalization.[14,15] Controllable experiments were conducted through the same method for the other two quinoline-bridged ionic COFs (QiCOFs), using vinyl sulfonate-based anionic ionic liquids (VAnILs) and vinyl imidazole-based cationic ionic liquids (VCaILs), with the corresponding samples named QAniCOF and QCaiCOF, respectively (Fig. 1a and S2).

We first conducted systematic density functional theory (DFT) computations to help unravel the ICT and dipole polarization in QiCOFs. The frontier molecular orbital distributions show that the lowest unoccupied molecular orbital (LUMO) electron density in all QiCOFs is predominantly localized on the quinoline backbone (Fig. 1b). Compared to the side-chain-free quinoline-linked COF (QCOF) (E_g = 3.44 eV), QZwiCOF shows a narrower band gap of 1.14 eV, with 2.44 eV and 1.85 eV obtained for QCaiCOF and QAniCOF, respectively. The obtained results suggest that the zwitterion can significantly improve ICT ability in QiCOFs.[16] Electrostatic potential (ESP) analysis reveals distinct charge distributions across the QiCOFs series. QCaiCOF displays intense positive potential at the imidazolium moiety with weaker positivity across the quinoline framework (Fig. 1c). Conversely, QAniCOF shows strong negative potential at the $-SO_3^-$ moiety and relatively moderate negativity along the quinoline backbone (Fig. 1d). For comparison, QZwiCOF exhibits a unique tripartite distribution, combining localized positive potential at the imidazolium site with negative potential at the $-SO_3^-$ group and quinoline backbone, creating a bidirectional dipole alignment (Fig. 1e). Quantitative ICT calculations suggest that an interionic charge transfer polarization,[17] *i.e.*, 0.19|*e*| transferred from sulfonate (δ−) to imidazolium (δ+), and a π-electron redistribution polarization, *i.e.*, 0.20|*e*| transferred from quinoline (δ−) to imidazolium (δ+) donation, exist in QZwiCOF (Fig. 1e and S3). While for QCaiCOF and QAniCOF, only one π-electron redistribution polarization is involved, in which 0.23|*e*| is donated from the electron-rich quinoline framework (δ−) to the imidazolium side chain (δ+) in QCaiCOF (Fig. 1c and S3), and 0.19|*e*| migrates from sulfonate groups (δ−) to the quinoline core (δ+) in QAniCOF (Fig. 1d and S3). Single-point energy calculations reveal a dipole moment of 27.22 debye for QZwiCOF, which is higher than those of QCaiCOF (19.34 debye), QAniCOF (25.69 debye) and side-chain-free QCOF (3.71 debye) (Fig. 1c–e).[18] These findings demonstrate that the unique extended π-conjugated zwitterionic structure endows QZwiCOF with enhanced charge transfer ability and dual polarization for a high dipole moment, which is expected to tune the structural regulation of PVDF-HFP.

Material structure characterization

In the Fourier transform infrared (FT-IR) spectra (Fig. 2a), the appearance of a characteristic absorption peak for the stretching vibration of the quinolyl group (1579 cm^{-1}), combined with the absence of characteristic absorption peaks for N–H stretching bands of TATT (3100–3400 cm^{-1}) and aldehyde group stretching bands of TATB (1700 cm^{-1}), confirms the successful occurrence of the Povarov reaction.[19,20] The disappearance of the peak signals at 920–960 cm^{-1}, attributed to the bending vibrations of the vinylene bonds in vinyl-based ionic liquids (VILs), verifies the successful modification of the third component onto the pore wall. In particular, the observed characteristic absorption peaks for $-SO_2-$ bonds from $-SO_3^-$ (1037 cm^{-1}) and imidazole groups (1604 cm^{-1}) in the as-prepared QZwiCOF suggests its amphiphilicity.[21] In the solid-state ^{13}C cross-polarization magic angle spinning nuclear magnetic resonance (CP-MAS ^{13}C NMR) spectra, the observed characteristic chemical shifts at 168 and 126 ppm, assigned to the carbon atoms of the triazine ring and benzene ring, and signals at 150, 159 ppm, attributed to the carbon atoms of the pyridinium ring, further indicate the formation of quinoline groups *via* the Povarov reaction.[22] While the observed characteristic signals for

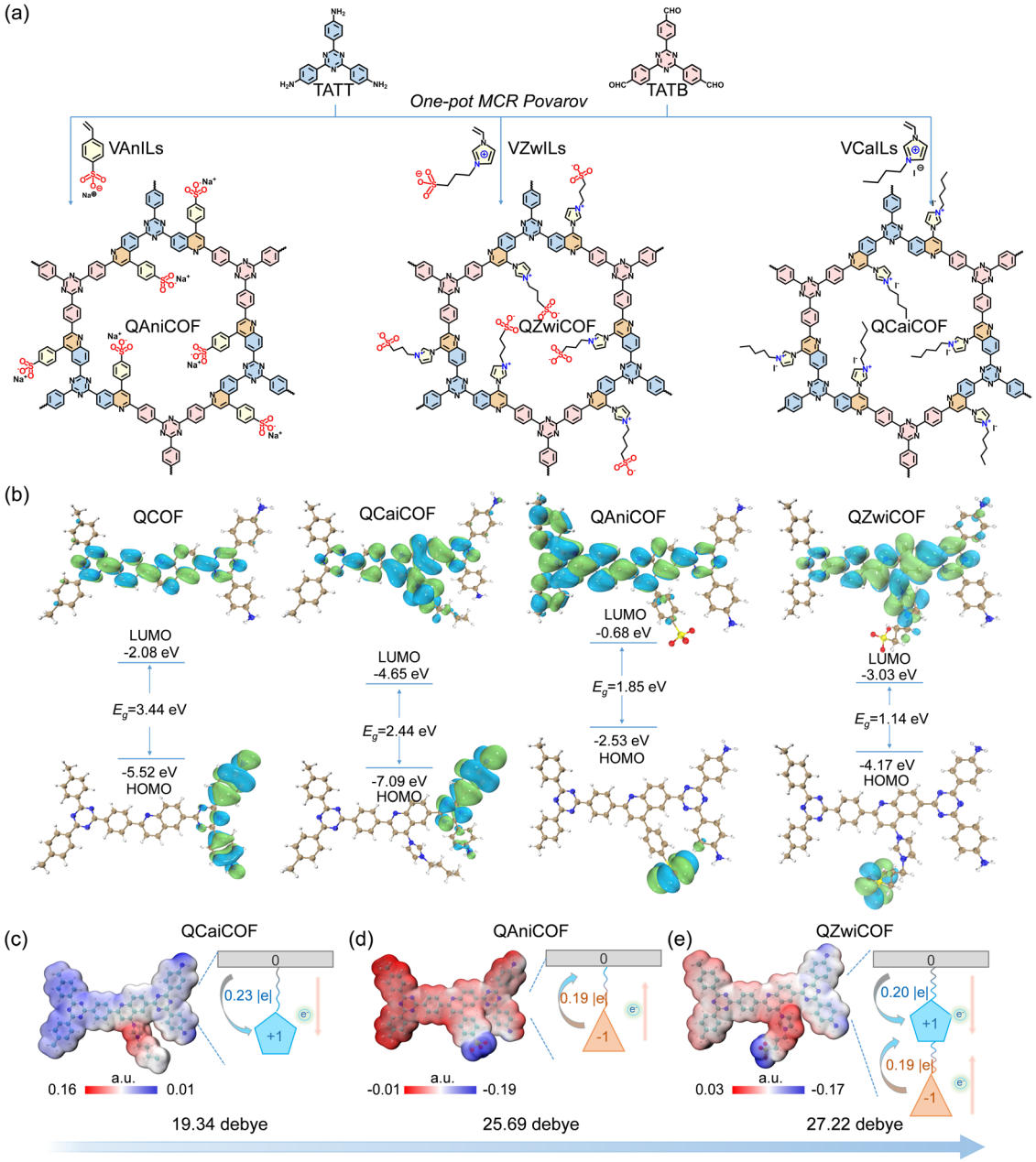

Fig. 1 Molecular design and DFT calculations. (a) Synthesis scheme of QAniCOF, QZwiCOF and QCaiCOF *via* a one-pot MCR Povarov reaction. (b) Frontier molecular orbital distributions of QCOF and QiCOFs. ESP distributions, ICT calculations and dipole moments for (c) QCaiCOF, (d) QAniCOF, and (e) QZwiCOF.

–CH_2– (19–50 ppm) further indicate the successful modification of pore walls (Fig. S6). Moreover, the observed binding energies at 401.8, 400.2 and 398.5 eV for imidazole N, quinoline N and triazine N in N 1s X-ray photoelectron spectroscopy (XPS), respectively, as well as the binding energies at 168.8 and 167.5 eV for SO_3^- in the S 2p XPS of QZwiCOF, support the successful synthesis of QZwiCOF (Fig. S7).[23] The relevant interpretations of structural characterization for QAniCOF and QCaiCOF can be found in the SI for details (Fig. S5–S9).

The observed characteristic diffraction peak in the X-ray diffraction (XRD) pattern, corresponding to the (100) reflection plane at a 2θ angle of 4.07°, indicates the formation of the expected crystalline layer structure for QZwiCOF. The simulation results support the experimental XRD pattern, with the ideal 2D crystalline structure obtained, exhibiting an eclipsed AA stacking arrangement along the c direction and lattice parameters of $a = b = 25.51$ Å, $c = 4.09$ Å (Fig. 2b). Additionally, the broad shoulder peak observed near ~20° indicates the presence of short-range ordered regions within the framework. This feature can be primarily attributed to the limited reversibility in the formation of highly conjugated quinoline linkers,[24] along with the presence of flexible ionic side

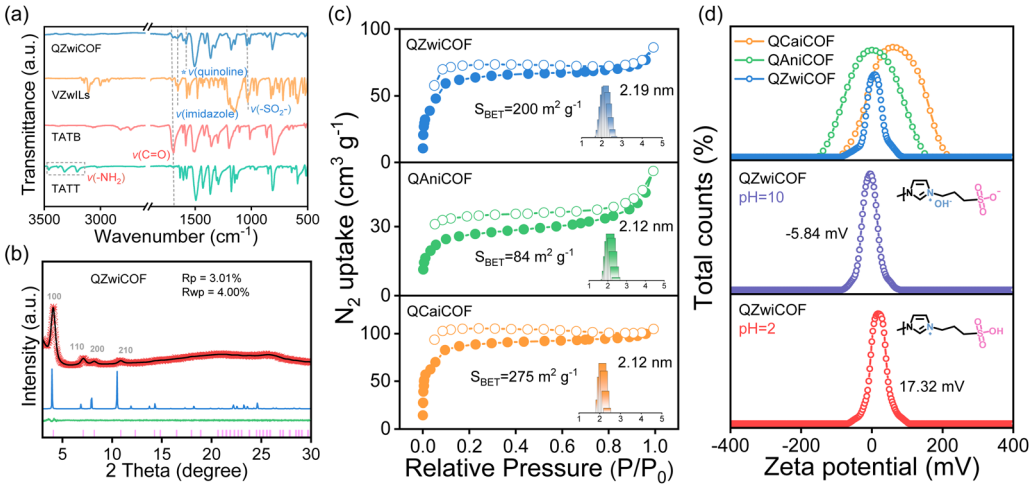

Fig. 2 Structural characterization of QiCOFs. (a) FT-IR spectra of QZwiCOF. (b) Experimental and simulated XRD patterns of QZwiCOF. (c) N_2 adsorption–desorption isotherms, with pore size distributions calculated by the NLDFT method for QiCOFs. (d) Mean zeta potential of QiCOFs dispersed in ethanol and mean zeta potential of QZwiCOF under varying pH conditions.

chains that may induce partial interlayer offsets.[25] The scanning electron microscopy (SEM) images show that all QiCOFs exhibit a branched rodlike morphology composed of aggregated crystallites (Fig. S11).[19] The high-resolution transmission electron microscopy (HR-TEM) images reveal the existence of lattice fringes with spacing around 3.8 Å for QZwiCOF (Fig. S12), which is close to the calculated interlayer distance in the AA structure (4.0 Å) (Fig. S13). Both SEM- and TEM-related micro-energy-dispersive spectroscopy (micro-EDS) elemental mapping images show that C N O S elements are homogeneously distributed in QZwiCOF (Fig. S14 and S15).[26] The observed Type-I model with a sharp uptake in the low relative pressure range (P/P_0 < 0.05) in the N_2 adsorption–desorption isotherms measured at 77 K suggests the microporous characteristics of QiCOFs (Fig. 2c). The Brunauer–Emmett–Teller (BET) specific surface area (S_{BET}) calculated from the sorption isotherms was 200 $m^2 g^{-1}$ for QZwiCOF, 84 $m^2 g^{-1}$ for QAniCOF, 275 $m^2 g^{-1}$ for QCaiCOF, with the average pore widths of 2.19, 2.12 and 2.12 nm, respectively (Fig. 2c inset and S16). The surface charge characteristics of the three QiCOFs were then investigated through zeta potential measurements at pH 7, which were 31.4, −23.6, and 0.76 mV for QCaiCOF, QAniCOF and QZwiCOF, respectively. Upon adjusting the pH value to 2 and 10, mean zeta potential values of 17.32 and −5.84 mV were achieved for QZwiCOF, respectively, verifying its amphiphilicity (Fig. 2d).[27] Moreover, the XRD patterns of QiCOFs almost maintained similar bulk crystallinity after immersion in DMAc solvent for 72 h (Fig. S18), illustrating their stable skeleton.[28]

Physicochemical properties and interaction analysis of electrolytes

The QiCOF-based electrolytes were prepared through an efficient slurry casting method; details can be found in Fig. 3a and the SI. Various weight ratios of QZwiCOF, including 1 wt%, 2 wt%, 3 wt%, 4 wt% and 5 wt%, were incorporated into PVDF-HFP (denoted as 1-ZiCP, 2-ZiCP, 3-ZiCP, 4-ZiCP, and 5-ZiCP, respectively). A denser morphology, a higher β-phase PVDF-HFP content, an increased concentration of free ions, and superior electrochemical properties were achieved for 3-ZiCP CPE (specific analysis can be found in the SI, Fig. S19–S27 and Table S3). We therefore selected 3 wt% QiCOFs to prepare CPEs for systematic investigation. As shown in the surface and cross-section SEM images (Fig. S28), the pure PVDF-HFP SPE exhibits a porous granular structure, whereas the iCP CPEs display a denser microsphere structure. This structural transition arises because QiCOF nanoparticles act as nucleating agents, promoting smaller spherulite formation and increased nucleation density that reduces inter-spherulite spacing.[29] The reduced spherulite size of iCP CPEs also triggers a fine-grain strengthening effect, and the well-ordered porous structures facilitate superior stress dispersion, which may collectively enhance the mechanical properties of electrolytes.[30] As depicted in stress–strain curves (Fig. 3b), the iCP CPEs exhibit higher mechanical performance, with stress values up to 4.20, 3.93, and 2.78 MPa, and high toughness values of 14.53, 7.73, 3.62 MJ m^{-3} for CiCP, ZiCP, AiCP CPEs, respectively. In contrast, PVDF-HFP SPE only shows a stress of 1.40 MPa and a toughness of 0.88 MJ m^{-3}. Thermal shrinkage experiments reveal that iCP CPEs also exhibit higher thermal stability, as no obviously dimensional shrinkage is observed even at 160 °C (Fig. 3c and S29). In addition, combustion tests indicate that QZwiCOF incorporation significantly enhances the electrolyte's flame resistance, thereby improving battery safety (Fig. S30). Further evaluation of a pure QZwiCOF pellet reveals exceptional flame retardancy, exhibiting immediate self-extinguishing behavior upon ignition (Fig. 3d). Remarkably, the pellet maintains structural integrity without deformation under prolonged flame exposure. This superior performance originates from the synergistic combination of nonflammable VZwILs within the rigid aromatic framework, which simultaneously enhances flame retardancy and shape retention.[31,32] Overall, these findings underscore that incorporating a small amount of QZwiCOF

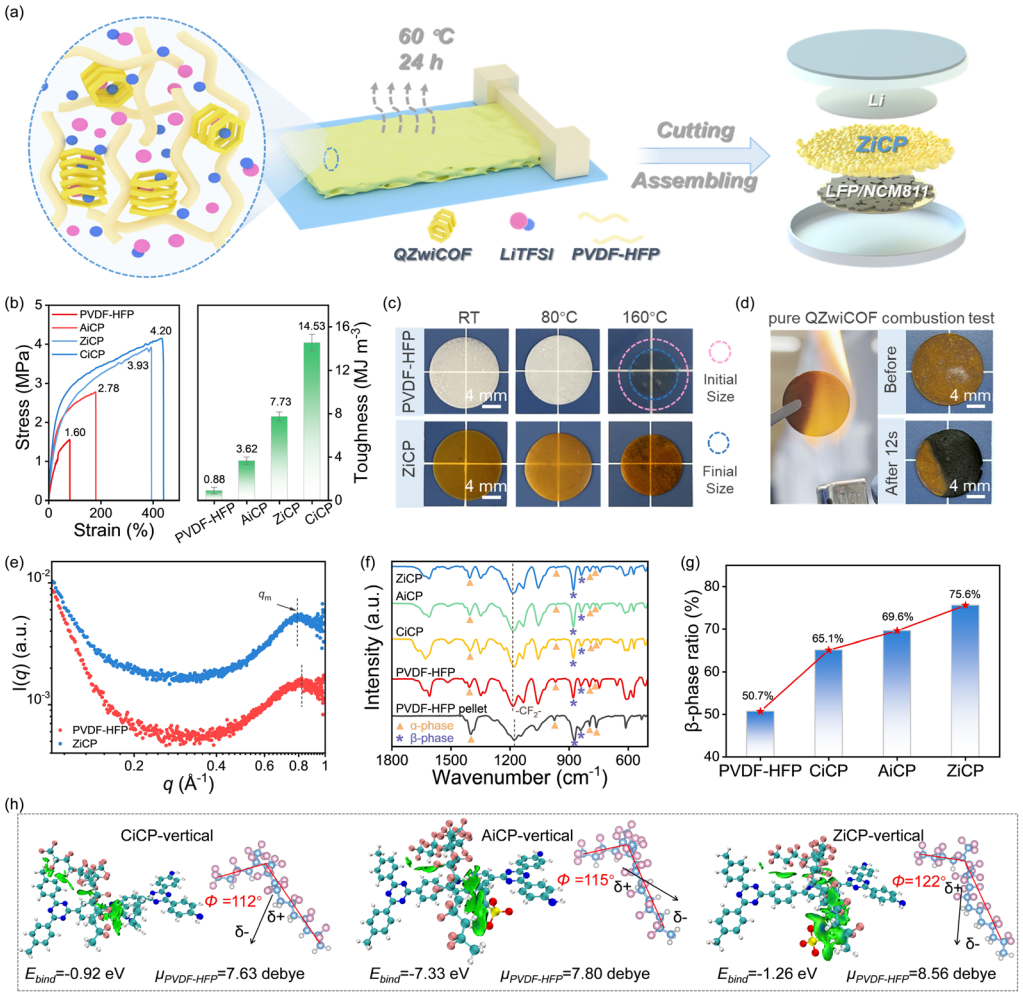

Fig. 3 Preparation and physicochemical properties of the electrolytes. (a) Schematic diagram of ZiCP CPE construction in SLMBs. (b) Typical stress–strain curves (left) and toughness (right) of electrolytes and (c) thermal shrinkage of PVDF-HFP SPE and ZiCP CPE after heating at different temperatures for 1 h. (d) Combustion test of a pure QZwiCOF pellet. (e) SAXS curves of PVDF-HFP SPE and ZiCP CPE, (f) FT-IR spectra and (g) calculated β-phase PVDF-HFP content of electrolytes based on the Lambert-Beer law. (h) Visualized with a density gradient isosurface of 0.002 a.u. in the IGMH analysis of iCP-vertical models.

into the PVDF-HFP matrix can significantly augment the mechanical strength and thermal stability.

By peak-fitting of XRD curves (Fig. S31 and Table S2), we can see that after incorporating QZwiCOF, the crystallinity degree (ΔX_c) of PVDF-HFP diminishes from 46% (PVDF-HFP SPE) to 33% (ZiCP CPE), providing a larger segmental motion free-volume. In ZiCP CPE, the TGTG conformations for the α-phase transform to a higher content of TTTT for the β-phase (65%), compared to merely 41% in PVDF-HFP SPE.[33] Small-angle X-ray scattering (SAXS) further confirms the increase in free volume of PVDF-HFP segments induced by QZwiCOF. As shown in Fig. 3e, the q_m of ZiCP CPE shifts towards to low-q region, and the corresponding d_m increases from 7.71 (PVDF-HFP SPE) to 8.01 Å (ZiCP CPE).[34] As shown in FT-IR spectra (Fig. 3f and S32), the intensity of peaks assigned to the crystalline phases (α-/β-phase) of PVDF-HFP SPE exhibits a notable decrease compared to pure PVDF-HFP pellets, further indicating the decrease in crystallinity. Based on the Lambert-Beer law, the average content of β-phase calculated from FT-IR adsorption spectra is 75.6% in ZiCP CPE, which is higher than that of PVDF-HFP SPE (50.7%) (Fig. 3g and Table S3). This is consistent with the trend observed in the XRD fitting results.[35] The parallel arrangement of dipoles in the β-phase is beneficial for providing more continuous ion transport channels.[36] To elucidate the interactions between QZwiCOF and PVDF-HFP, FT-IR spectra with varying QZwiCOF contents were recorded. The blue shift of the $-CH_2$ group in PVDF-HFP from 1400 cm^{-1} to 1405 cm^{-1} indicates a change in the stretched vibrational state of the VDF segments induced by QZwiCOF. Similarly, the blue shift of the $-CF_2-$ stretching vibration peak from 1167 cm^{-1} to 1181 cm^{-1} suggests dipole interactions between QZwiCOF and PVDF-HFP[37] (Fig. S33a). These observed shifts in the scattering peaks of $-CH_2$ at 1431 cm^{-1} and 2986 cm^{-1} to 1414 cm^{-1} and 2976 cm^{-1}, respectively, were further supported by Raman spectra[38] (Fig. S33b). The larger free volume of the chain segments, coupled with the regular dipole arrangement,

is expected to significantly enhance ion migration within the polymer matrix.

DFT computational results demonstrate that all composite systems induce significant dipolar rearrangement in PVDF-HFP chains, with dihedral angles (Φ) increasing from 99° in the pristine state to 102–122°, accompanied by dipole moment ($\mu_{\text{PVDF-HFP}}$) enhancement from 6.80 debye to 7.69–8.56 debye (Fig. 3h, S34 and 35). Notably, owing to the dual polarization in QZwiCOF, PVDF-HFP achieves both the largest Φ of 122° and the largest $\mu_{\text{PVDF-HFP}}$ of 8.56 debye in the vertically aligned model. Hirshfeld partition (IGMH) analysis reveals dominant dipole interactions between QiCOFs and PVDF-HFP (green isosurfaces) in both horizontal and vertical orientations, demonstrating that the dual polarization enforces aligned orientation of C–F dipoles through interfacial electrostatic forces.[39] Particularly, in ZiCP, the dual polarization exerts dual effects through the flexible VZwILs side chain, driving C–F bond rotation along the polarization direction, significantly enhancing the dipole moment ($\Delta\mu$ = +1.76 debye *vs.* pristine). Energy minimization calculations show a marked preference for different PVDF-HFP alignments, with an E_{bind} of −1.26 eV for vertical and −0.58 eV for horizontal in ZiCP, −7.33 eV for vertical and −6.79 eV for horizontal in AiCP, and −0.92 eV for vertical and −0.60 eV for horizontal in CiCP, indicating thermodynamically favored orthogonal chain packing in the iCP CPEs. Moreover, molecular dynamics (MD) trajectories demonstrate the dynamic equilibrium between parallel and perpendicular PVDF-HFP orientations on the (001) plane of QZwiCOF (Fig. S36), establishing both configurations as genuine representations of polymorphic chain packing in iCP CPEs. Collectively, these results demonstrate that dual polarization in QZwiCOF induces PVDF-HFP structural reorganization into more ordered, high-dipole configurations through dipole interactions, which are expected to simultaneously optimize ion-pair dissociation and uniform ion transport for higher σ.

Electrochemical properties and mechanism analysis

We then evaluated the electrochemical properties of these electrolytes. As illustrated in Fig. 4a, S37 and Table S6, the calculated σ values of PVDF-HFP SPE, CiCP, AiCP and ZiCP CPEs, based on electrochemical impedance spectroscopy (EIS) measurements at 30 °C, are 1.59×10^{-5}, 5.05×10^{-5}, 1.54×10^{-4} and 3.44×10^{-4} S cm^{-1}, respectively. The enhanced σ originates from QiCOF-induced dipole alignment in PVDF-HFP, which establishes continuous and oriented ion transport pathways. The t_{Li^+} of PVDF-HFP SPE, CiCP, AiCP and ZiCP CPEs, assessed through direct current (DC) polarization and alternating current (AC) impedance measurements, is 0.27, 0.34, 0.54 and 0.56, respectively (Fig. S38), with σ_{Li^+} individually contributing 0.43×10^{-5}, 1.72×10^{-5}, 8.32×10^{-5} and 1.93×10^{-4} S cm^{-1}, respectively. It can be seen that ZiCP CPE exhibits the highest σ and t_{Li^+}, followed by AiCP and CiCP CPEs. The markedly improved t_{Li^+} of ZiCP CPE arises from the unique dual polarization of the functional additive QZwiCOF, which significantly enhances both $\mu_{\text{PVDF-HFP}}$ and the planar regularity of PVDF-HFP, thereby promoting the establishment of highly efficient ion transport pathways. The calculated lowest activation energy (E_a) of 0.23 eV from Arrhenius plots reveals that the lowest migration barrier for Li^+ transport in ZiCP CPE, followed by 0.28, 0.39 and 0.51 eV for AiCP, CiCP CPEs and PVDF-HFP SPE, respectively (Fig. 4b, S39 and S40). This observation can be attributed to the effective dissociation of TTTT conformation PVDF-HFP with enhanced $\mu_{\text{PVDF-HFP}}$ and partially selective Li^+-conduction within QZwiCOF, as supported by the above experimental and simulation analyses. Notably, the measured electrochemical stability window (ESW) of ZiCP and AiCP CPEs can be extended to 4.9 V, followed by 4.8 and 4.7 V for CiCP CPE and PVDF-HFP SPE, based on linear sweep voltammetry (LSV) tests (Fig. 4c). The significantly widened ESW of ZiCP and AiCP CPEs may stem from the elevated $\mu_{\text{PVDF-HFP}}$, which strengthens charge delocalization, consequently lowering the HOMO energy level (−8.74 eV for PVDF-HFP in ZiCP, −8.72 eV for PVDF-HFP in AiCP) and broadens the E_g (8.58 eV for PVDF-HFP in ZiCP and 8.52 eV for PVDF-HFP in AiCP) (Fig. S41).[40] These effects collectively endow the electrolytes with improved oxidation stability and electron-insulating properties. Furthermore, owing to the highest σ_{Li^+} and t_{Li^+}, the ZiCP CPE delivered a higher critical current density (CCD) of 2.7 mA cm^{-2} compared to 2.1 mA cm^{-2} for PVDF-HFP SPE (Fig. 4d). Compared with the reported PVDF-HFP based SPEs, the abovementioned electrochemical properties of ZiCP CPE are competitive (Fig. 4e and Table S7).[41–47]

To understand the coordination environment of Li^+ in electrolytes, a series of characterization studies were conducted. Based on the characteristic peak around 745 cm^{-1} in Raman spectra (Fig. S43 and S44), the relative proportion of free ions (sum of C_1 and C_2) for ZiCP CPE is calculated to be 88%, exceeding the 76% observed for PVDF-HFP SPE.[48] In the ^{7}Li solid-state nuclear magnetic resonance (^{7}Li ss-NMR) spectra (Fig. 4f), the downfield shift of the ^{7}Li resonance peak in ZiCP CPE indicates greater ion-pair dissociation ability within ZiCP CPE.[49] Similarly, C 1s and F 1s XPS spectra confirm the presence of less undissociated LiTFSI in ZiCP CPE (Fig. S45). These observations can be attributed to the increased TTTT-PVDF-HFP within ZiCP CPE, which enhances the local $\mu_{\text{PVDF-HFP}}$ and consequently weakens the coulombic interaction between Li^+ and $TFSI^-$ through stronger electrostatic effects, facilitating lithium salt dissociation.[33]

It should be mentioned that the amphiphilic nanochannels in QZwiCOF may also play a partial role in the improved σ, as further evidenced by DFT calculations and MD simulations presented in Fig. S46 and S47. As the snapshots show (0 to 20 ps), Li^+ in ZiCP CPE migrates *via* a dual mechanism, *i.e.*, hopping along dipoles within polymer chain gaps and traversing the pores of QZwiCOF. In contrast, Li^+ in PVDF-HFP SPE follows a single migration pathway. Notably, magnified trajectories highlight the bonding method of Li^+ during its migration in ZiCP CPE (Fig. 4g). Initially, Li^+ is closer to the N atom of $TFSI^-$ (5.13 Å) than to the F in PVDF-HFP (7.99 Å). At t = 10 ps, the Li–F (PVDF-HFP) distance (3.59 Å) becomes shorter than the Li–O (TFSI) distance (5.40 Å). By t = 20 ps, as Li^+ migrates into QZwiCOF channels, the Li–O (–SO_3^-) distance

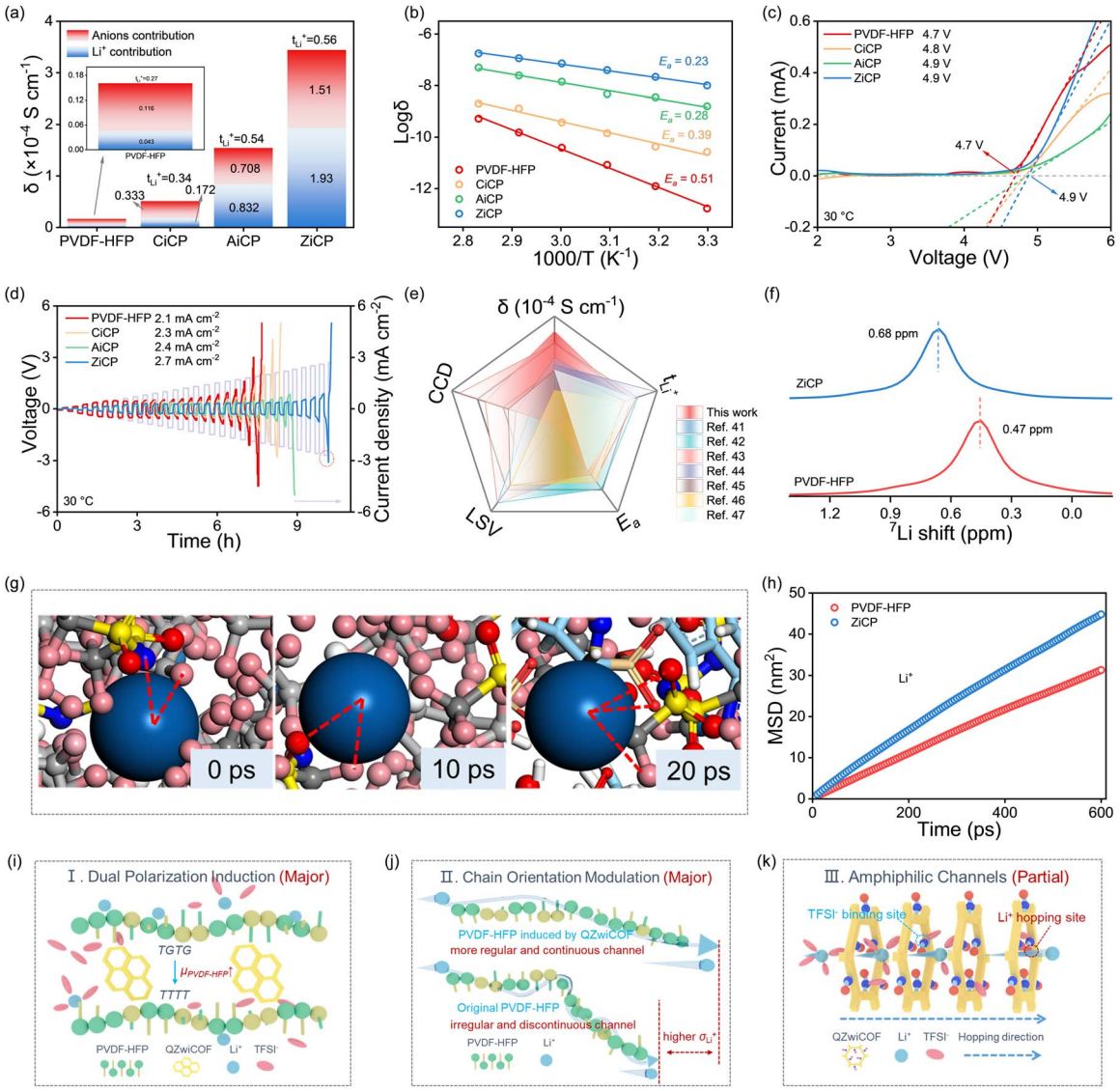

Fig. 4 Electrochemical performance and theoretical calculations of ions transport behavior in electrolytes. (a) The ionic conductivities, Li^+ transference numbers and Li^+ conductivity contribution, (b) activation energy, (c) electrochemical stability window and (d) critical current density of electrolytes. (e) Comparison of the electrochemical performance of the reported PVDF-based SPEs. (f) ^7Li ss-NMR of PVDF-HFP SPE, ZiCP CPE. (g) Partially enlarged Li^+ chemical environment diagrams in ZiCP ($t = 0$, 10, 20 ps), where dark blue represents Li, blue corresponds to N, pink indicates F, red designates O, and yellow symbolizes S. (h) Calculated MSD of Li^+ in PVDF-HFP SPE and ZiCP CPE. Schematics for the multiple functions of QZwiCOF to facilitate Li^+ dissociation and migration: (i) dual polarization induction, (j) chain orientation modulation, and (k) amphiphilic channels.

(6.57 Å) is significantly shorter than the Li–F (PVDF-HFP) distance (9.80 Å) and Li–O ($TFSI^-$) distance (10.67 Å). These results confirm stronger Li–F interactions during hopping in PVDF-HFP, while Li^+ interacts predominantly with $-SO_3^-$ groups within the molecular channels.[50,51] From the time evolution of the mean square displacement (MSD), Li^+ diffusion in ZiCP CPE is significantly faster than in PVDF-HFP SPE, while the diffusion of $TFSI^-$ anions is constrained in ZiCP CPE (Fig. 4h and S48). This indicates that QZwiCOF enhances Li^+ mobility while suppressing $TFSI^-$ movement, consistent with the observed electrochemical properties.

Through comprehensive analysis, we elucidate the multifunctional role of QZwiCOF in enhancing ZiCP CPE performance *via* three synergistic mechanisms. First, the dual polarization of QZwiCOF induces dipole realignment in PVDF-HFP, promoting the formation of highly ordered TTTT conformations with enhanced $\mu_{PVDF\text{-}HFP}$. This structural reorganization facilitates lithium salt dissociation through strengthened local $\mu_{PVDF\text{-}HFP}$ (Fig. 4i). Second, the more ordered chain orientation of PVDF-HFP establishes aligned pathways for Li^+ transport, significantly improving the σ (Fig. 4j). Third, the amphiphilic channels leverage synergistic sulfonate–imidazolium interactions to provide Li^+ hopping sites while electrostatically restricting anion migration through coulombic trapping effects, thereby creating a selective Li^+ conduction channel (Fig. 4k). This multiscale synergistic regulation strategy

ultimately enables the ZiCP CPE to achieve simultaneous breakthroughs in electrochemical performance.

Li deposition performance and SEI analysis

The assembled symmetric Li||Li cells were operated to investigate the Li plating and stripping behaviors. The Tafel polarization demonstrates superior ionic transport kinetics in the ZiCP CPE-based symmetric Li||Li cell, exhibiting an exchange current density (i_0) of 0.30 mA cm^{-2}, significantly higher than that of AiCP (0.25 mA cm^{-2}), CiCP (0.21 mA cm^{-2}), and PVDF-HFP SPE (0.15 mA cm^{-2}) based cells (Fig. 5a).[52] This enhanced ionic transport capability directly correlates with reduced interfacial polarization during charge/discharge cycles.[53] Corresponding galvanostatic cycling tests (Fig. 5b) further confirm this advantage, with the Li||ZiCP CPE||Li cell maintaining exceptional stability for over 1000 h at 0.2 mA cm^{-2} while sustaining a slim polarization voltage of only 50 mV. By contrast, the assembled Li||PVDF-HFP SPE||Li cell displays a high polarization voltage of 115 mV and cycles for <20 h before short-circuiting. Even under current densities of 0.5 and 1.0 mA cm^{-2}, the ZiCP CPE still shows better stability than PVDF-HFP SPE (Fig. S49a and b). More inspiringly, the Li||ZiCP CPE||Li cell still shows a lower polarization voltage of 30 mV under 1.0 mA cm^{-2} at 80 °C, and exhibits the lifetime of more than 100 h (Fig. S49c). The lower and more stable polarization voltage of ZiCP CPE probably benefits from the multi regulation channels and accelerated Li^+ migration kinetics. Moreover, the reversible Li plating and stripping performance was measured at increasing current densities from 0.05 to 1.0 mA cm^{-2} (Fig. S49d). The overpotential of Li||ZiCP CPE||Li remains consistently low at 17, 40, 70, 130 and 213 mV, respectively, while Li||Li cells with AiCP CPE possess higher polarization voltage than those with ZiCP CPE. In contrast, the symmetric Li cells with CiCP CPE and PVDF-HFP SPE only last at 1.0 and 0.5 mA cm^{-2}, respectively. Compared with previously reported PVDF-based SPEs (Table S8), the ZiCP CPE exhibits a lower and more stable polarization voltage under the same current density, indicating satisfactory interfacial compatibility with Li metal. The interfacial contact resistance (R_{int}) of electrolytes against Li metal was evaluated using distribution of relaxation times (DRT) analysis.[54] As shown in Fig. 5c, the R_{int} of Li||ZiCP CPE||Li gradually reduced over 50, 100, 200, 300, and 400 cycles, which can be attributed to the presence of a stable solid electrolyte interphase (SEI) that connects the solid–solid interface between the electrolyte and Li electrode.

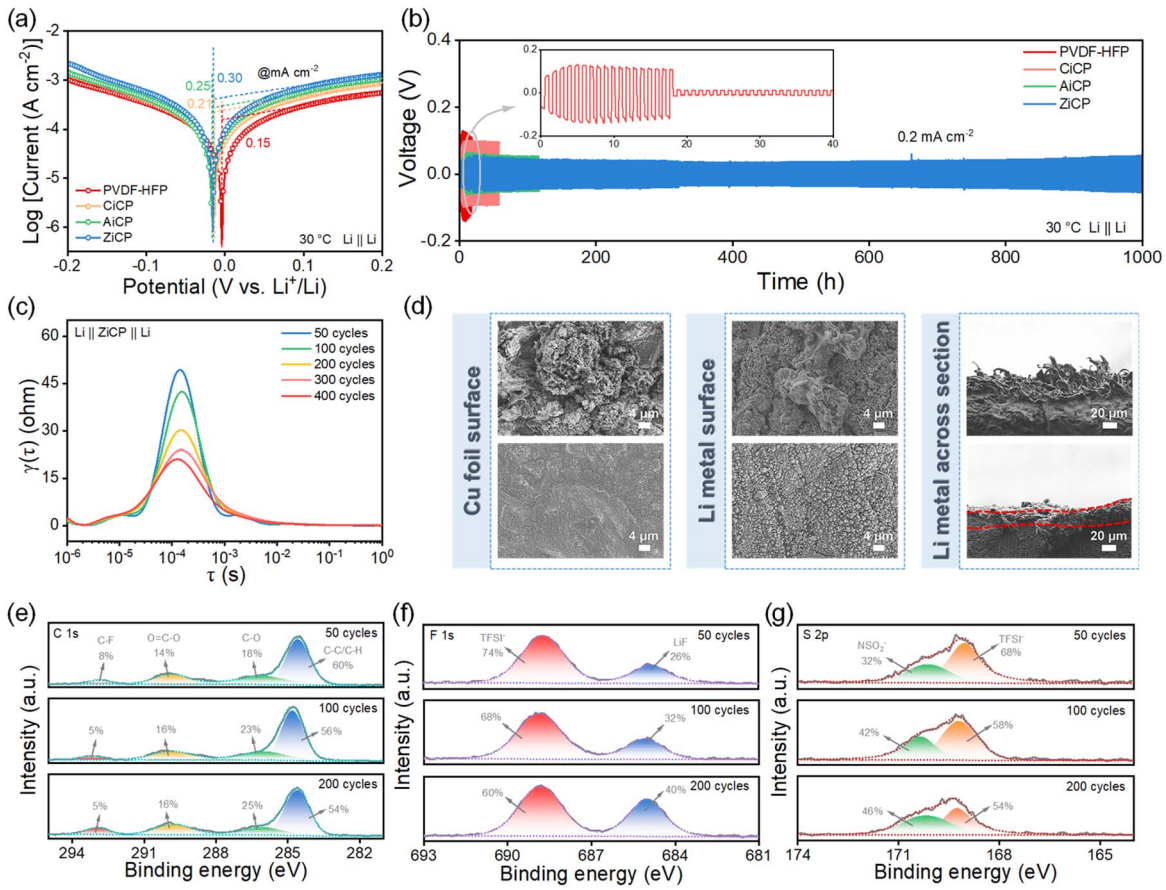

Fig. 5 Characterization of Li deposition performance and the SEI layer. (a) Tafel curves of Li||Li cells. (b) Galvanostatic cycling curves of Li||Li cells at a current density of 0.2 mA cm^{-2}. (c) DRT curves of the Li||ZiCP CPE||Li cell at different cycles. (d) SEM images of the Cu foil surface, Li surface and Li cross-section for Li||Cu cells with PVDF-HFP SPE (up) and ZiCP CPE (down) after 20 cycles at 0.2 mA cm^{-2}. (e–g) XPS spectra of the Li metal in cycled Li||ZiCP CPE||Li cells.

To evaluate the morphological evolution of the interfacial layer during lithium deposition, the Li‖Cu half cells with PVDF-HFP SPE and ZiCP CPE were assembled to deposit Li on Cu foil after 20 cycles at the current density of 0.2 mA cm^{-2}. After Li platting/stripping, the SEM images of the ZiCP CPE@Cu foil surface show that Li particles are uniformly and continuously distributed on the surface of Cu foil, while the PVDF-HFP SPE@Cu foil surface exhibits large Li agglomerates. Similarly, the surface and cross section of PVDF-HFP SPE@Li metal exhibit uneven whisker-like lithium dendrites and substantial voids within the deposited layer. In contrast, the ZiCP CPE facilitates remarkably uniform and dense lithium deposition, forming a smooth layer approximately 15 μm thick, entirely free of dendritic features (Fig. 5d).[55] Furthermore, the ZiCP CPE-based cell demonstrates significantly enhanced coulombic efficiency, maintaining 97.05% after 20 cycles, with a slight increase from the initial efficiency of 96.09%. This performance starkly contrasts with that of the PVDF-HFP SPE-based cell, which exhibits a considerable decline from 92.48% to 86.82% over the same cycling period (Fig. S50). Furthermore, the morphological evolution of the Li metal surface during deposition in the ZiCP CPE system was directly monitored *via in situ* optical microscopy. As shown in Fig. S51, the Li deposition layer maintains a flat and smooth surface throughout the entire 60 min plating process at a current density of 0.5 mA cm^{-2}. The above results demonstrate that the ZiCP CPE facilitates highly homogeneous lithium deposition, which may be attributed to its well-ordered multi-channel ion transport pathways. After that, the chemical composition of the SEI between ZiCP CPE and Li metal was investigated by XPS analysis.[56] As depicted in Fig. 5e–g, there are four peaks at 284.6, 286.0, 289.8 and 293.0 eV assigned to C–C/C–H, C–O, O–C=O and C–F in C 1s, respectively. With cycling progression, the relative intensities of C–C/C–H and C–F decreased, while those of C–O and C–C=O increased, indicating Li_2CO_3 formation and suppressed $TFSI^-$ accumulation. Similarly, the F 1s (688.8 eV) and S 2p (169.2 eV) spectra confirm the inhibition of $TFSI^-$ accumulation. The appearance of LiF (685.0 eV) contributes to an electronically insulating shielding layer, enhancing the mechanical properties of the SEI. The generation of Li_2CO_3, LiF and sulfide components in the SEI endows the ZiCP CPE with enhanced electrochemical stability and mechanical ductility against lithium dendrites. These observations align with Sand's kinetic equation,[57] where enhanced Li^+ conductivity and selectivity reduce concentration polarization, facilitating homogeneous SEI formation. This effectively suppresses lithium dendrite formation and extends battery lifespan.

Electrochemical performance of SLMBs

The enhanced Li^+ electrochemical migration and favorable electrochemical deposition within ZiCP CPE are validated by SLMBs. First, Li‖$LiFePO_4$ (LFP) cells were assembled. As shown in Fig. S52a–c, the Li‖ZiCP CPE‖LFP cell displays favorable rate stability with the specific capacities of 185, 175, 163, 150 and 128 mAh g^{-1} at 0.1, 0.2, 0.5, 1.0 and 2.0C, respectively. Especially, the specific capacity recovers to 178 mAh g^{-1} and remains stable as the rate returns to 0.1C. In contrast, the Li‖PVDF-HFP SPE‖LFP cell delivered lower specific capacities of 168, 163, 150, 120 and 89 mAh g^{-1} at the same rate and when the rate returned to 0.1C, the discharge capacity decreased continuously. Furthermore, the Li‖ZiCP CPE‖LFP delivered a specific capacity of 157 mAh g^{-1} with a capacity retention of 66.7% after 200 cycles at a rate of 1.0C, while the Li‖PVDF-HFP SPE‖LFP cell retained only 39.1% (Fig. S52d). These results demonstrate that improved Li^+ migration and better interfacial affinity accelerate the electrode reaction kinetics.

To verify the adaptability to next-generation high-voltage cathode material $LiNi_{0.8}Co_{0.1}Mn_{0.1}O_2$ (NCM811), Li‖NCM811 cells were assembled. As shown in Fig. 6a, the rate specific capacities of the Li‖ZiCP CPE‖NCM811 cell are 226, 215, 200, 185, 164 and 145 mAh g^{-1} at 0.1, 0.2, 0.5, 1.0, 2.0 and 3.0C, respectively, which are much higher than those of Li‖PVDF-HFP SPE‖NCM811 (163, 156, 137, 109, 76, and 51 mAh g^{-1}, respectively). The charge/discharge curves reveal that the Li‖PVDF-HFP SPE‖NCM811 cell exhibits a significant capacity decay at high C-rates, mainly due to its lower t_{Li^+}, which increases concentration polarization near the NCM811 cathode (Fig. 6b). In particular, in terms of rate performance, the Li‖NCM811 cell assembled with ZiCP CPE significantly outperforms those with AiCP CPE (62 mAh g^{-1}), CiCP CPE (54 mAh g^{-1}), and PVDF-HFP SPE (51 mAh g^{-1}) at a high rate of 3.0C (Fig. S53a). Similarly, the Li‖ZiCP CPE‖NCM811 cell exhibits an outstanding initial capacity of 166 mAh g^{-1} at 1.0C, retaining a specific capacity of 137 mAh g^{-1} with a capacity retention of 82.5% after 200 cycles, much higher than the 36.0% observed for the Li‖PVDF-HFP SPE‖NCM811 cell (Fig. 6c). And the cell demonstrates long-term cycling stability, maintaining a specific capacity of 104.4 mAh g^{-1} after 700 cycles at 0.2C (Fig. S53b). Even under extreme operating conditions, the cell assembled with ZiCP CPE shows excellent performance retention, achieving a specific capacity of 108 mAh g^{-1} with a capacity retention rate of 87.8% after 200 cycles at 3.0C, while the other cells with AiCP, CiCP CPEs and PVDF-HFP SPE experience a short-circuit within 10 cycles (Fig. 6d and S53c). Meanwhile, the cell retains a capacity of 96 mAh g^{-1} after 200 cycles at an elevated temperature of 80 °C and a high rate of 6.0C, while the cell with PVDF-HFP SPE experiences a short circuit within 50 cycles (Fig. 6e). It is important to emphasize that the initial capacity degradation may be attributed to the consumption of active lithium during the formation of the SEI.[58] Furthermore, the persistent coulombic efficiency below 99.90% throughout cycling may result from structural degradation of the NCM811 cathode under high temperature and high current density conditions.[59] These results unambiguously demonstrate the superior rate capability and high-temperature stability of the ZiCP CPE, attributed to its reduced polarization and enhanced Li^+ transport kinetics enabled by the unique QZwiCOF-induced electrolyte architecture. As revealed by the EIS analysis in Fig. S54, after 100 cycles, the charge transfer resistance (R_{ct}) of the Li‖PVDF-HFP SPE‖NCM811 cell increased sharply from 53.2 Ω to 105.1 Ω, while that of the ZiCP CPE-based cell only rose from 31.3 Ω to 59.2 Ω. This pronounced contrast clearly demonstrates the better interfacial compatibility and reduced polarization

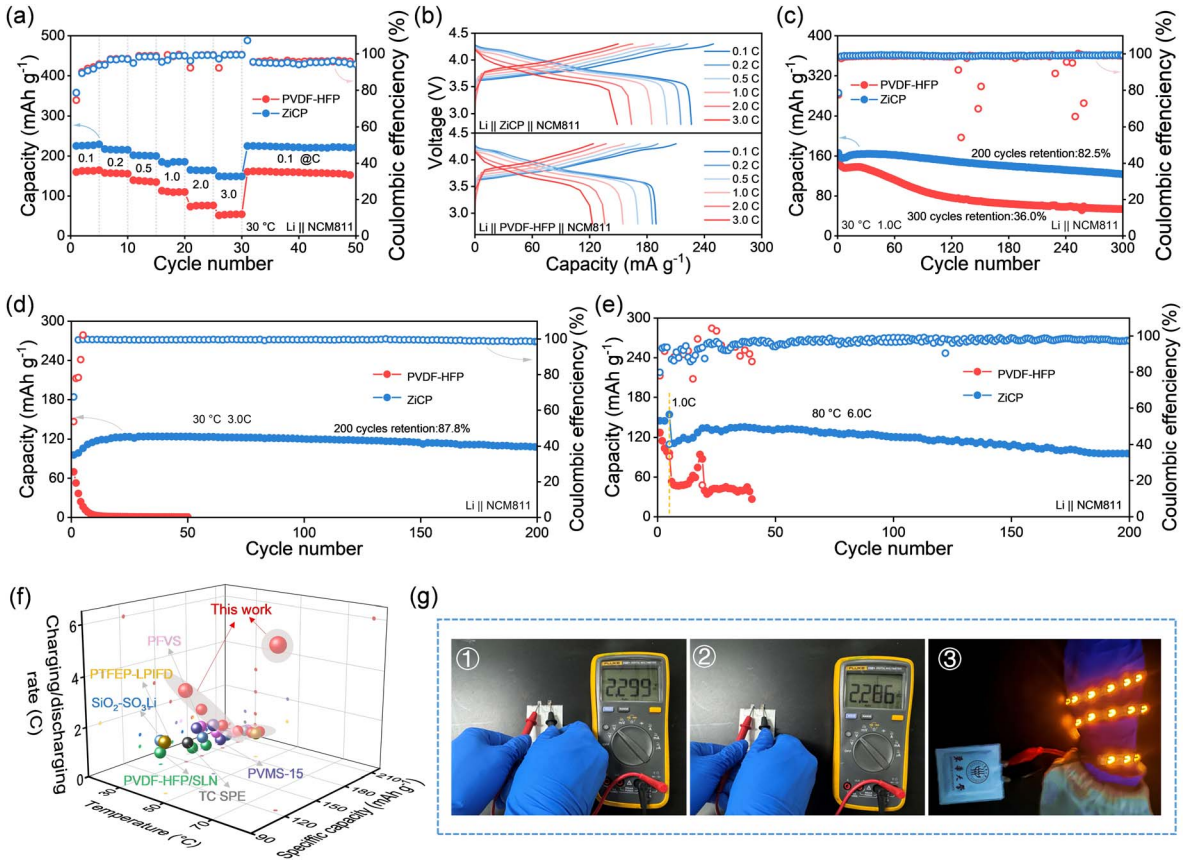

Fig. 6 Electrochemical performance of PVDF-HFP-based solid-state Li metal batteries. (a) The rate performance of Li||NCM811 cells from 0.1C to 3.0C (1C = 200 mAh cm^{-2}). (b) Charge and discharge voltage profiles of Li||NCM811 cells at different rates. (c and d) Cycling performance of the Li||NCM811 cells at 1.0C and 3.0C, respectively. (e) Cycling performance of the Li||NCM811 cells at 6.0C, 80 °C (first activated 5 cycles with 1.0C). (f) Cycle performance comparison of reported Li||NCM811 cells in different SPE-LMBs. (g) Open-circuit voltage and LED bulb illumination demonstrated by the Li||ZiCP CPE||LFP pouch cell.

enabled by the ZiCP CPE.[60] Compared with the reported PVDF-based SPEs in recent years as mentioned in Fig. 6f and Table S9,[35,42–44,61,62] the ZiCP CPE in this work shows both excellent cycling and rate performance in the Li||NCM811 cell.

In order to validate the potential application of ZiCP CPE in the commercial field, a high loading-mass NCM811 (~9.2 mg cm^{-2}) cathode was used to measure the cycling performance of the full battery. As shown in Fig. S53d, the Li||NCM811 cell exhibits 71.6% capacity retention after 180 cycles at 0.1C. To further confirm the applicability, a flexible solid-state Li pouch cell (Li||LFP) was constructed and used to power an LED bulb. As shown in Fig. 6g, the open-circuit voltage of the pouch cell could reach 2.29 V with no obvious loss after long-time storage, which is high enough to turn on an LED bulb. These above results demonstrate the promising potential of QZwiCOF as a regulator doped in the PVDF-HFP matrix for application in high-performance SLMBs.

Conclusions

In summary, we demonstrate a multipolar molecular engineering strategy for high-performance composite polymer electrolytes through the rational design of QZwiCOF. The extended π-conjugated QZwiCOF, synthesized *via* a one-pot Povarov reaction, induces dual polarization that simultaneously enforces PVDF-HFP dipole alignment ($\mu_{PVDF\text{-}HFP}$ = 8.56 debye) and chain planarization ($\Delta\Phi$ = +23°), while enabling selective Li^+ transport through amphiphilic nanochannels. The resulting electrolyte (ZiCP CPE) enables high σ (3.44 × 10^{-4} S cm^{-1}), a high t_{Li^+} (0.56), exceptional mechanical strength (3.93 MPa) and flame retardancy. Benefiting from outstanding thermal and electrochemical stability, the Li||NCM811 cell assembled with ZiCP CPE shows excellent rate performance, especially at a 3.0C-rate, delivering a high specific capacity of 145 mAh g^{-1}, and outperforming cells with AiCP CPE (62 mAh g^{-1}), CiCP CPE (54 mAh g^{-1}), and PVDF-HFP SPE (51 mAh g^{-1}). During 3.0C charge–discharge cycling, the cell exhibits a specific capacity of 108 mAh g^{-1} with a capacity retention of 87.8% after 200 cycles. Even under more stringent conditions of 80 °C and 6.0C, it retains a capacity of 96 mAh g^{-1} after 200 cycles, while the cell with PVDF-HFP SPE experiences a short circuit within 50 cycles. This work establishes a molecular-level design principle for high-performance solid-state batteries through precisely engineered polarization effects in COF-based composite electrolytes.

Author contributions

W. L. and Y. Z. L. supervised the project, provided funding to conduct the work and conceived the idea. L. C. X. and F. C. performed the experiments and wrote the draft. J. D. and J. Z. W performed the experiments. K. X. W and J. Q. L helped to revise the manuscript. J. N. W joined the discussion of the data and gave helpful suggestions. All authors contributed to the discussion and final version of the manuscript.

Conflicts of interest

There are no conflicts of interest to declare.

Data availability

The data supporting this article have been included as part of the SI.

Supporting information: additional information about materials preparations (synthesis and characterization methods, fabrication of cells and electrochemical measurements), supplementary figures (supplementary characterization of QiCOFs, supplementary characterization of electrolytes, supplementary properties of the electrolytes), supplementary tables (supplementary data of QiCOFs and electrolytes, performance comparison of electrolytes). See DOI: **https://doi.org/10.1039/d5sc05645d**.

Acknowledgements

The authors acknowledge the financial support from the National Natural Science Foundation of China (52373172, 52073046, and 52473055), the National Key Research and Development Program of China (2022YFB3807100 and 2022YFB3807102), the Program of Shanghai Academic Research Leader (21XD1420200), the Chang Jiang Scholar Program (T2023082), the Natural Science Foundation of Shanghai (23ZR1401100), the Key Technology Research and Development Program of Shanghai (25CL2900800), the State Key Laboratory for Modification of Chemical Fibers and Polymer Materials (KF2204, KF2306, and KF2316), and the Fundamental Research Funds for the Central Universities (CUSF-DH-T-2024023).

References

1 J. Janek and W. G. Zeier, *Nat. Energy*, 2016, **1**, 16141.
2 W. Li, M. Li, S. Wang, P. H. Chien, J. Luo, J. Fu, X. Lin, G. King, R. Feng and J. Wang, *Nat. Nanotechnol.*, 2025, **20**, 265–275.
3 Z. Ning, G. Li, D. L. Melvin, Y. Chen, J. Bu, D. Spencer Jolly, J. Liu, B. Hu, X. Gao and J. Perera, *Nature*, 2023, **618**, 287–293.
4 Z. Song, F. Chen, M. Martinez Ibaez, W. Feng, M. Forsyth, Z. Zhou, M. Armand and H. Zhang, *Nat. Commun.*, 2023, **14**, 4884.
5 V. Fleury, *Nature*, 1997, **390**, 145–148.
6 S. Li, H. Hong, D. Li, X. Yang, S. Wang, D. Zhang, Q. Xiong, Z. Huang and C. Zhi, *Angew. Chem., Int. Ed.*, 2025, **64**, e202409500.
7 R. Chang, Y. Liu, Y. Zhang, Y. Shi, J. Tang, Z.-L. Xu, X. Zhou and J. Yang, *Adv. Energy Mater.*, 2025, 2405906.
8 D. You, Z. Lai, W. Wei and H. Xiong, *Adv. Funct. Mater.*, 2025, **35**, 2415464.
9 H. Shantao, W. Peng, W. Huaijiao, Z. Yang, G. Yu, Z. Lu, S. H. Yang, L. Xinrong and C. Mao, *Nat. Mater.*, 2023, **22**, 1515–1522.
10 K. Hashimoto, T. Shiwaku, H. Aoki, H. Yokoyama, K. Mayumi and K. Ito, *Sci. Adv.*, 2023, **9**, 9.
11 W. Zhang, V. Koverga, S. Liu, J. Zhou, J. Wang, P. Bai, S. Tan, N. K. Dandu, Z. Wang and F. Chen, *Nat. Energy*, 2024, **9**, 15.
12 J. Song, L. Lin, F. Cui, H. G. Wang, Y. Tian and G. Zhu, *Chem. Sci.*, 2024, **15**, 11480–11487.
13 Y. Ma, Y. Qiu, K. Yang, S. Lv, Y. Li, X. An, G. Xiao, Z. Han, Y. Ma and L. Chen, *Energy Environ. Sci.*, 2024, **17**, 8274–8283.
14 J. Duan, F. Chen, H. Yu, S. Zhu, L. Teng, K. Wang, T. Chen, W. Lyu, H. Hu and Y. Liao, *Angew. Chem., Int. Ed.*, 2025, e202505207.
15 Y. Li, J. Duan, Y. Wang, L. Teng, H. Liu, J. Li, M. Liu, W. He, H. Hu, L. Wang, W. Lyu and Y. Liao, *Chem. Sci.*, 2025, **16**, 11311–11321.
16 X. Mi, J. Li, W. Lyu, L. Xu, Y. Liu, C. Qian, J. Yu, W. He, J. Feng and Y. Liao, *Appl. Catal., B*, 2025, **378**, 125530.
17 K. Xiong, X. Jia, Y. Kong, J. Yang, J. Guo, S. Li, M. Adeli, Y. Wang, X. Luo, X. Han and C. Cheng, *Adv. Funct. Mater.*, 2025, 2510257.
18 Z. Chen, J. Guo, F. H. Song, S. D. Wang, S. A. C. Carabineiro, S. X. Ouyang and L.-L. Wen, *ACS Catal.*, 2025, **15**, 8284–8296.
19 P. Das, J. Roeser and A. Thomas, *Angew. Chem., Int. Ed.*, 2023, **135**, e202304349.
20 S. Cao, A. Zhang, H. Fang, B. Feng, Y. Liu, P. Yi, S. He, Z. Ren, L. Ma, W. Lu, M. Ye and J. Shen, *Energy Environ. Sci.*, 2025, **18**, 3395–3406.
21 Z. Zhang and Y. Xu, *J. Am. Chem. Soc.*, 2023, **145**, 25222–25232.
22 B. J. Yao, W. X. Wu, L. G. Ding and Y. B. Dong, *J. Org. Chem.*, 2021, **86**, 3024–3032.
23 R. Zhang, Z. D. Yang, Y. Yang, F. M. Zhang and G. Zhang, *ACS Appl. Mater. Interfaces*, 2023, **15**, 57265–57272.
24 Y. Zhao, H. Liu, C. Wu, Z. Zhang, Q. Pan, F. Hu, R. Wang, P. Li, X. Huang and Z. Li, *Angew. Chem., Int. Ed.*, 2019, **58**, 5376–5381.
25 R. Xia, X. Zheng, C. Li, X. Yuan, J. Wang, Z. Xie and X. Jing, *ACS Nano*, 2021, **15**, 7638–7648.
26 J. Lee, J. Lee and J. Seo, *Nat. Commun.*, 2024, **15**, 8688.
27 Y. Fu, Y. Wu, S. Chen, W. Zhang, Y. Zhang, T. Yan, B. Yang and H. Ma, *ACS Nano*, 2021, **15**, 19743–19755.
28 C. Qian, W. Zhou, J. Qiao, D. Wang, X. Li, W. L. Teo, X. Shi, H. Wu, J. Di and H. Wang, *J. Am. Chem. Soc.*, 2020, **142**, 18138–18149.
29 Z. Li, Y. Zheng, C. Liao, S. Duan, X. Liu, G. Chen, L. Dong, J. Dong, C. Ma and B. Yin, *Adv. Funct. Mater.*, 2024, **34**, 2404427.

30 P. Zhai, Z. Yang, Y. Wei, X. Guo and Y. Gong, *Adv. Energy Mater.*, 2022, **12**, 2200967.
31 S. Li, F. Pei, Y. Ding, X. Guo, X. Zhang, H. Tao, Z. He, H. Hu and L. Zhang, *Adv. Funct. Mater.*, 2024, **35**, 2415495.
32 J. Hwang, K. Matsumoto, C. Y. Chen and R. Hagiwara, *Energy Environ. Sci.*, 2021, **14**, 5834–5863.
33 C. Dai, M. Weng, B. Cai, J. Liu, S. Guo, H. Xu, L. Yao, F. J. Stadler, Z. M. Li and Y. F. Huang, *Energy Environ. Sci.*, 2024, **17**, 8243–8253.
34 C. M. Wu and S. Y. Lin, *J. Phys. Chem. C*, 2015, **119**, 12335–12344.
35 Q. Wu, M. Fang, S. Jiao, S. Li, S. Zhang, Z. Shen, S. Mao, J. Mao, J. Zhang, Y. Tan, K. Shen, J. Lv, W. Hu, Y. He and Y. Lu, *Nat. Commun.*, 2023, **14**, 6296.
36 S. Wang, C. Li, Y. Ma, H. Zhang, X. Shi, L. Zhang and D. Song, *Angew. Chem., Int. Ed.*, 2024, **64**, e202420698.
37 Y. Cao, T. G. Morrissey, E. Acome, S. I. Allec, B. M. Wong, C. Keplinger and C. Wang, *Adv. Mater.*, 2017, **29**, 1605099.
38 B. Yang, C. Deng, N. Chen, F. Zhang, K. Hu, B. Gui, L. Zhao, F. Wu and R. Chen, *Adv. Mater.*, 2024, **36**, 2403078.
39 J. Li, W. Lyu, X. Mi, C. Qian, Y. Liu, J. Yu, R. B. Kaner and Y. Liao, *Adv. Sci.*, 2024, **11**, 2401966.
40 M. Li, H. An, Y. Song, Q. Liu, J. Wang, H. Huo, S. Lou and J. Wang, *J. Am. Chem. Soc.*, 2023, **145**, 25632–25642.
41 L. Liu, Y. Shi, M. Liu, Q. Zhong, Y. Chen, B. Li, Z. Li, T. Zhang, H. Su and J. Peng, *Adv. Funct. Mater.*, 2024, **34**, 2403154.
42 K. Liu, H. Cheng, Z. Wang, Y. Zhao, Y. Lv, L. Shi, X. Cai, Z. Cheng, H. Zhang and S. Yuan, *Adv. Energy Mater.*, 2024, **14**, 2303940.
43 W. Zhang, V. Koverga, S. Liu, J. Zhou, J. Wang, P. Bai, S. Tan, N. K. Dandu, Z. Wang and F. Chen, *Nat. Energy*, 2024, **9**, 386–400.
44 S. Xia, B. Yang, H. Zhang, J. Yang, W. Liu and S. Zheng, *Adv. Funct. Mater.*, 2021, **31**, 2101168.
45 Z. Ding, Q. Tang, Q. Zhang, P. Yao, X. Liu and J. Wu, *Nano Res.*, 2023, **16**, 9443–9452.
46 W. Liu, C. Yi, L. Li, S. Liu, Q. Gui, D. Ba, Y. Li, D. Peng and J. Liu, *Angew. Chem., Int. Ed.*, 2021, **60**, 12931–12940.
47 J. Sun, X. Yao, Y. Li, Q. Zhang, C. Hou, Q. Shi and H. Wang, *Adv. Energy Mater.*, 2020, **10**, 2000709.
48 W. Huang, S. Wang, X. Zhang, Y. Kang, H. Zhang, N. Deng, Y. Liang and H. Pang, *Adv. Mater.*, 2023, **35**, 2310147.
49 Q. Xia, H. Kaixin, X. Ma, P. Qiu, Z. Li and X. Chen, *Chem. Sci.*, 2024, **15**, 17579–17589.
50 Y. Xiang, N. Yu, J. Li, H. Xu, S. Chen, Y. Xia, Z. Luo, X. Li, Z. Liu and M. Xu, *Angew. Chem., Int. Ed.*, 2025, e202424288.
51 P. Liu, X. Y. Kong, L. Jiang and L. Wen, *Chem. Soc. Rev.*, 2024, **53**, 2972–3001.
52 Y. Liguo, W. Xinying, C. Li, D. Shen, Z. Shao, H. Wu, S. Xiao, W. Liang, Y. Yu and Y. Li, *Energy Environ. Sci.*, 2024, **17**, 1117–1131.
53 Q. Lv, L. Li, X. Zhang, R. Wang, N. Wen, L. Xue, H. Wang, L. Shen, D. Chen and F. Ciucci, *J. Am. Chem. Soc.*, 2025, **147**, 27611–27623.
54 Y. Chen, X. Gao, Z. Zhen, X. Chen, L. Huang, D. Zhou, T. Hu, B. Ren, R. Xu and J. Chen, *Energy Environ. Sci.*, 2024, **17**, 9288–9302.
55 X. Li, J. Feng, Y. Li, N. Li, X. Jia, Y. Wang and S. Ding, *Energy Storage Mater.*, 2024, **72**, 103759.
56 H. Peng, T. Long, J. Peng, H. Chen, L. Ji, H. Sun, L. Huang and S. G. Sun, *Adv. Energy Mater.*, 2024, **14**, 2400428.
57 C. Brissot, M. Rosso and J. N. Chazalviel, *J. Power Sources*, 1999, **81**, 925–929.
58 P. M. Attia, S. Das, S. J. Harris, M. Z. Bazant and W. C. Chueh, *J. Electrochem. Soc.*, 2019, **166**, E97–E106.
59 X. G. Yang, T. Liu, Y. Gao, S. Ge and C. Y. Wang, *Joule*, 2019, **3**, 3002–3019.
60 Y. Ma, L. Chen, Y. Li, B. Li, X. An, X. Cheng, H. Su, K. Yang, G. Xiao and Y. Zhao, *Energy Environ. Sci.*, 2025, **18**, 3730–3739.
61 L. Zhao, Q. Dong, Y. Wang, G. Xue, X. Wang, Z. Li, H. Shao, H. Chen, Y. Shen and L. Chen, *Angew. Chem., Int. Ed.*, 2024, **63**, e202412280.
62 Y. F. Huang, J. P. Zeng, S. F. Li, C. Dai, J. F. Liu, C. Liu and Y. B. He, *Adv. Energy Mater.*, 2023, **13**, 2203888.